UCLA

UCLA Electronic Theses and Dissertations

Title

Voltage-Controlled Magnetic Anisotropy in Heavy Metal|Ferromagnet|Insulator-Based Structures

Permalink

Author

Li, Xiang

Publication Date

2015

Peer reviewed|Thesis/dissertation

UNIVERSITY OF CALIFORNIA

Los Angeles

Voltage-Controlled Magnetic Anisotropy

in Heavy Metal|Ferromagnet|Insulator-Based Structures

A thesis submitted in partial satisfaction

of the requirements for the degree Master of Science

in Electrical Engineering

by

Xiang Li

2016

ABSTRACT OF THE THESIS

Voltage-Controlled Magnetic Anisotropy

in Heavy Metal|Ferromagnet|Insulator-Based Structures

by

Xiang Li

Master of Science in Electrical Engineering

University of California, Los Angeles, 2016

Professor Kang Lung Wang, Chair

Electric-field assisted writing of magnetic memory that exploits the voltage-controlled magnetic anisotropy (VCMA) effect offers a great potential for high density and low power applications. Magnetoelectric Random Access Memory (MeRAM) has been investigated due to its lower switching current, compared with traditional current-controlled devices utilizing spin transfer torque (STT) or spin-orbit torque (SOT) for magnetization switching. It is of great promise to integrate MeRAM into the advanced CMOS back-end-of-line (BEOL) processes for on-chip embedded applications, and enable non-volatile electronic systems with low static power dissipation and instant-on operation capability.

In this thesis, different heavy metal|ferromagnet|insulator-based structures are grown by magnetron sputtering to improve the VCMA effect over the traditional Ta|CoFeB|MgO-based

structures. We also established an accurate measurement technique for VCMA characterization. An improved thermal annealing stability of VCMA over 400°C is achieved in Mo|CoFeB|MgO-based structures. In addition, we observed a weak CoFeB thickness dependence of both VCMA coefficient and interfacial perpendicular magnetic anisotropy (PMA) in both Ta|CoFeB|MgO and Mo|CoFeB|MgO-based structures.

The thesis of Xiang Li is approved.

Oscar M. Stafsudd

Jane Pei-Chen Chang

Kang Lung Wang, Committee Chair

University of California, Los Angeles

2016

To my family, my love, and my dream

On the Road

Table of Contents

List of Figures

List of Tables

ACKNOWLEDGEMENTS

First of all, I would like to thank Prof. Kang L. Wang for taking me into the DRL group. His grand vision of the field of nanoelectronics from the fundamental point of view impressed me a lot, for which I will try my best to inherit later on in my PhD career. Setting high goals and implementing them is also one of his most admirable traits. The passion, perseverance, insight, and hard work he demonstrated will always be a high standard I strive for in my future life. I would also like to thank his care, guidance, and shared wisdom to me in everyday's encounters.

Secondly, I would like to thank my co-advisor, Prof. Pedram Khalili Amiri, who is not officially my advisor, but effectively guided me through the major portion of my experimental work shown in this thesis. It is the big picture he envisioned that attracted me into working on this project. Among various discussions, he always gave a practical and insightful engineering perspective that linked my experimental work with the real problems for further commercialization of the technology we are researching on.

Thirdly, I would like to thank Dr. Guoqiang Yu for supporting and guiding me through various small experimental details. I would always remember the time we spent together in the sputtering room discussing various strategies to tackle a problem. More importantly, his perspective in choosing important directions for research while managing different projects simultaneously will benefit me forever. I would also like to thank him for helping me out in countless occasions in my life and being so nice and helpful along the way.

Next, gratitude will be given to Dr. Qi Hu for guiding me and teaching me how to be a good engineer in the first half year of my research on thin film development. The strategy, reasoning, and professionalism that I learnt from him will be indispensable for my future career.

I want to also thank people in the spintronics group for helping me out along the way: Juan Alzate, his hospitality and enthusiasm opened the door of spintronics to me, and I still missed the welcoming atmosphere while he was here; Kin Wong, his brilliant humor and great professionalism make him the most accountable in our group and I must thank him for fabricating those lot of devices. Also, I would like to thank Mustafa Akyol, Farbod Ebrahimi, Xue Qing Cai, Cecile Grezes, Pramey Upadhyaya, Mohsen Yazdani, Minghua Li, Wenyuan Li for all your support!

Being at DRL is actually only part of my experience of my Master degree. I also had close interaction with Diana Chien from Prof. Jane P. Chang's lab in the Department of Chemical Engineering. We have been through ups and downs in our collaboration and I would always thank her enthusiasm, optimism and help in this process. I would also like to thank all in the TANMS community where I have made precious friends as well as lot of publications. The interdisciplinary nature of the TANMS center definitely helped my communication and leadership skills which are invaluable for a graduate student.

I would sincerely like to thank Prof. Jane P. Chang and Prof. Oscar Stafsudd for taking the time and effort to go through my thesis and providing valuable advices and comments. Acknowledgement also goes to TANMS and the FAME center for funding my research.

Finally, the emotional and financial support from my parents, grandparents, uncle, my fiancé and my future parents-in-law is indispensable for me to go through the whole process of graduate career. In addition, teachers, staff, and friends I met both here at UCLA and from other places gave me huge power to go forward and realize my dream.

Chapter 1: Introduction

1.1 Memory hierarchy

In the present memory hierarchy, a wide range of memory technologies have occupied different application spaces based on their different performance attributes, as shown in *Figure 1*.[1] Typically static random access memory (SRAM) serves as CPU register and cache (L1-L3), dynamic random access memory (DRAM) as the main working memory, flash as portable and integrated storage for consumer electronics, and magnetic hard disk as high-density storage used in data centers. At one end of this spectrum, DRAM possesses faster speed and lower dynamic power consumption, however requires constant refreshing of data due to its volatile nature. While at the other end of the spectrum, flash and hard disk drive demonstrate non-volatility thus can retain data after power if off, but they sacrifice with much lower access speed and rather large energy consumption for read and write operations. Apart from power-delay considerations, cost and capacity are equally important factors in considering the memory hierarchy. As SRAM and DRAM are rather expensive to process with a rather low areal density, they normally are offered in rather capacity suitable for on-chip memory applications. On the other hand, the flash drive and hard disk drive can achieve low cost as well as high density thus becoming premium for long term data storage. Hence, there lacks a universal memory which provides both high access speed and low dynamic power consumption comparable to SRAM and DRAM, as well as the non-volatile nature for minimal static power consumption, high areal density and capacity as shown in flash and hard disk drives.

There indeed have been intensive research on new type of non-volatile memory technologies to realize a universal memory, such as spin transfer torque magnetic random access memory (STT-MRAM), phase change random access memory (PCRAM), and resistive random access memory (RRAM), among others. However, it can be imagined that it should be rather difficult to develop one technology that has all advantages required for the universal memory: smaller power consumption than SRAM, comparable latency to SRAM, non-volatile retention comparable to flash, higher density than DRAM, and last but not the least, lower cost than DRAM. Considering that SRAM and DRAM technologies are still constantly improving with very low development cost, it remains challenging for any emerging technology to deliver such promised merits in an efficient and cost-effective way.
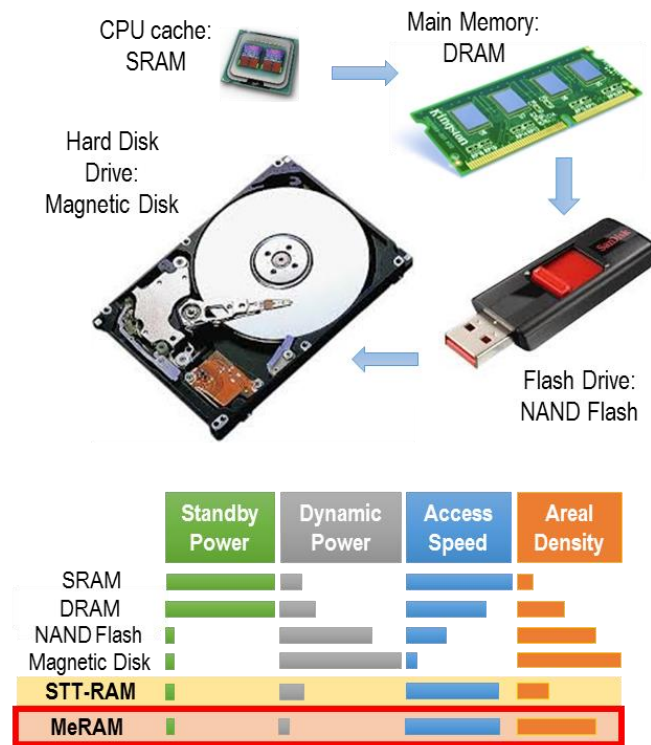
Figure 1. Memory hierarchy including SRAM, DRAM, NAND flash, magnetic disk which are in market, as well as STT-RAM and MeRAM which are still in development stage.

1.2 Magnetoelectric random access memory (MeRAM) as embedded memory

As seen in *Table 1*, magnetoelectric random access memory (MeRAM) which is the main focus of this thesis, is indeed promising to realize this stringent requirement for universal memory. Especially, the dynamic power consumption of MeRAM can be two orders of magnitude lower than SRAM and STT-RAM, while it can maintain comparable write and read access speed to that of SRAM. It has comparable density with DRAM and extremely high endurance ($>10^{15}$ cycles). However, the major drawback for MeRAM application is the cost as industry needs to integrate magnetic materials and related processes into the standard fabrication line.

Table 1. Comparison of existing and emerging memory technologies, highlighting STT-MRAM (using current-induced switching) and MeRAM (using electric-field-controlled switching). [1]

Technology	SRAM	DRAM	NAND Flash	STT-MRAM	MeRAM
Energy/bit (fJ)	100	1,000	10^6	**100**	**≤ 1**
Write Speed (ns)	1	20	10^6	**1-10**	**1-10**
Read Speed (ns)	1	30	50	**1-10**	**1-10**
Density (area in F^2)	>30	6-10	4	**8-30**	**4-8**
Endurance (cycles)	Very High	Very High	Low	**Very High**	**Very High**
Nonvolatility	No	No	Yes	**Yes**	**Yes**
Standby Power	Leakage Current	Leakage Current	None	**None**	**None**
Cost overhead vs. CMOS	Large area (6T)	Separate process	Separate process	**Back-end-of-line (BEOL) process**	**Back-end-of-line (BEOL) process**
Nonvolatile Logic Capability	No	No	No	**Very limited due to power**	**Yes**

In a more realistic review of the application opportunities of MeRAM technology, embedded memory applications for system-on-chips (SoCs) seem to be a rather feasible route to achieve wide range commercialization of this novel technology. As embedded memories are utilized in a wide variety of application conditions, there exists a potential for MeRAM to tailor its design to meet the specific requirement for various applications. These requirements are usually less stringent than commodity stand-alone memories. To date, the density of these SoCs embedded memories are usually limited from kilobits to tens of megabits,[2] due to the limited density of SRAM.

Different from DRAM and flash technologies, the STT-RAM and MeRAM technologies are compatible with CMOS back-end-of-line (BEOL) process, which makes it convenient to be integrated into SoCs. Moreover, compared with existing embedded flash and DRAM technologies, MeRAM need fewer masks than embedded flash during processing, thus reducing the cost possibly. Last, embedded flash needs high gate voltage which results in additional overhead, and embedded DRAM requires extremely high aspect-ratio capacitor to keep the cell capacitance.

1.3 Voltage-controlled magnetic anisotropy

Present MRAM devices typically utilize current-controlled switching of magnetization via the spin transfer torque (STT)[3,4] or spin-orbit torque (SOT)[5,6] effects to write information into magnetic bits. However, the use of currents results in a memory cell size (i.e. bit density) limitation due to the large size of the required access transistors,[7,8] and large dynamic switching energy due to Ohmic power dissipation. Writing of information using electric field in perpendicular magnetic tunnel junctions (MTJs)[9-12] is being investigated intensively, with the goal of realizing energy-efficient and high density Magnetoelectric Random Access Memory (MeRAM) devices.[1,13,14] The

4

electric-field effect, or the voltage-controlled magnetic anisotropy (VCMA) effect, is utilized to temporarily lower the interfacial perpendicular magnetic anisotropy (PMA) of the free layer during the writing operation, thus reducing the writing energy required to overcome the energy barrier between the two stable magnetization states, as shown in *Figure 2*.[1,13]

As indicated from *ab initio* calculations, the interfacial PMA in K_i stems from the hybridization of Fe/Co *3d* orbitals and O *2p* orbitals at the CoFeB/MgO interface.[15,16] The application of positive electric field (i.e. top electrode of MTJ at higher electric potential) across the MgO barrier will induce the depletion of electrons at the CoFeB/MgO interface, which will decrease the occupancy of electrons in Fe d_{xz}, d_{yz} orbitals and enhance the occupancy in Fe d_{xy} orbitals. As higher density of d_{xz}, d_{yz} orbitals leads to a larger PMA, the application of a positive electric field produces a lower K_i.
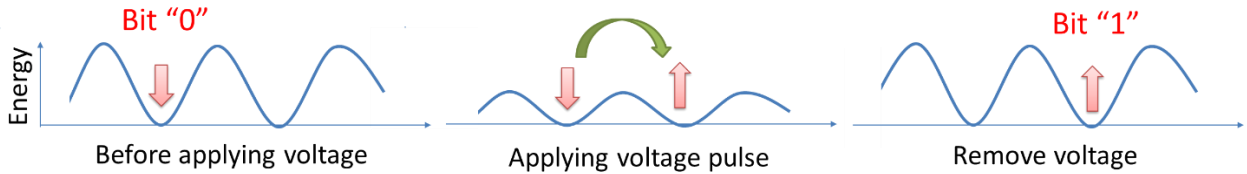
Figure 2. Schematic showing the process of magnetization switching using voltage-controlled magnetic anisotropy effect. External forces such as magnetic field or spin transfer torque are required to switch the magnetization during the voltage pulse period.

Particularly, various heavy metal|CoFeB|MgO material systems have been investigated intensively as they have several advantages: high tunneling magnetoresistance (TMR) for reading,[17,18] perpendicular magnetic anisotropy (PMA) for high density and scaling,[19-25] and voltage-controlled magnetic anisotropy (VCMA) for energy-efficient writing.[1-7,24-29] As discussed in the previous sections, it is also highly desirable to further integrate embedded MeRAM into

CMOS logic circuits to achieve non-volatile electronic systems with low standby power and instant-on operation capability,[7,30] which requires the compatibility with the thermal budget of CMOS back-end-of-line process. In addition, as the CoFeB thickness is a very important design parameter for MeRAM applications, it is also of great interest to investigate the CoFeB thickness dependence of VCMA effect using an accurate electrical transport measurement technique.

In this thesis, we first demonstrate higher VCMA and PMA thermal annealing stability in annealed Mo|CoFeB|MgO layered structures over Ta|CoFeB|MgO structures.[31] The interfacial PMA is observed to increase with annealing over the studied temperature range, and a VCMA coefficient of about 40 fJ/V-m is sustained after annealing at temperatures as high as 430°C. *Ab initio* electronic structure calculations of interfacial PMA as a function of strain further show that strain relaxation may lead to the increase of the interfacial PMA at higher annealing temperatures. The measurement data also show that there is no significant VCMA and interfacial PMA dependence on the CoFeB thickness over the studied range, illustrating the interfacial origin of the anisotropy and its voltage dependence, i.e. the VCMA effect. The high thermal annealing stability of Mo|CoFeB|MgO structures makes them compatible with advanced CMOS back-end-of-line processes, and will be important for integration of MeRAM into on-chip embedded applications.

Next, we will investigate the CoFeB thickness dependence of VCMA coefficients in Ta|CoFeB|MgO-based structures using three different VCMA characterization techniques, from which we will establish one accurate measurement and data analysis method. In particular, the dependence of VCMA effect on ferromagnetic layer thickness is studied for perpendicular Ta|CoFeB|MgO-based Hall bars and magnetic tunnel junctions (MTJs). Hard-axis *R-H* loops under different applied voltages are performed to extract the change of the interfacial perpendicular

anisotropy as function of electric field, i.e. the VCMA coefficient. To obtain the interfacial PMA value under one specific applied electric field, the *R-H* loop under this applied electric field has to be normalized into an *M-H* loop. In this normalization process, one has to determine at least two anomalous Hall and/or MTJ resistance ($R_{\text{Hall}}/R_{\text{MTJ}}$) values under each applied electric field to be referenced to specific perpendicular component of magnetization (M_{Z}) values (e.g. $M_{\text{Z}} = 0, \pm M_{\text{S}}$). We compare the CoFeB thickness dependent VCMA effect using two normalization methods to convert $R_{\text{Hall}}/R_{\text{MTJ}}$ values into the perpendicular component of magnetization M_{Z} in the VCMA calculations. Using an "individual" normalization method where the reference values of $R_{\text{Hall}}/R_{\text{MTJ}}$ are determined to be different for each applied electric field results in a strong CoFeB thickness dependent VCMA effect. However, if an "overall" normalization method considering the same reference value of R_{Hall} for different applied electric field cases is used, a weak VCMA dependence on CoFeB thickness over the studied range is obtained. The multi-domain behavior at perpendicular to in-plane transition region is also discussed. The knowledge obtained through this study is fundamental for a proper characterization of the VCMA strength of different materials.

Chapter 2: Thermally stable voltage-controlled perpendicular magnetic anisotropy in Mo|CoFeB|MgO structures

2.1 Motivation

In the commonly used Ta|CoFeB|MgO system, the PMA and TMR cannot be sustained when an annealing temperature above 400°C is used,[32,33] making it incompatible with advanced CMOS back-end-of-line processes, where metallic interconnects and low-k dielectrics used between the interconnects require a thermal budget over 400°C.[34,35] Several works have recently explored MTJs with improved thermally stable TMR and PMA for STT-MRAM applications, primarily by blocking or eliminating Ta diffusion under high temperatures.[34-37] Nevertheless, for VCMA-based embedded memory applications, it is critical to develop new material systems that can also provide thermally stable VCMA after annealing at 400°C.

A possible route to achieve this goal is to exploit the effect of the metal seed (or cap) layer on the PMA[25,38,39] and VCMA in MTJ structures.[25,27-29] Only recently, there have been reports on improving the thermal stability of PMA, TMR and VCMA in MTJs by changing the Ta-based material stacks to Mo|CoFeB|MgO[21,22,40] and W|CoFeB|MgO.[23,24] However, a detailed study on the thermal stability of VCMA in the Mo|CoFeB|MgO material system, particularly after annealing above 400°C, is still needed.

Here we present a detailed study on the effect of annealing on PMA, saturation magnetization (M_S), and VCMA in Mo|CoFeB|MgO film stacks. A VCMA coefficient (ξ) of 40 fJ/V-m is demonstrated after annealing at 430°C for 30 minutes.[41] We also observe a higher ξ of 50 fJ/V-m at lower annealing temperature (T_A) of 360°C. These VCMA coefficients are

comparable to the best high-temperature VCMA (>400°C) values (40-50 fJ/V-m) reported to date for W-based samples in Ref. [24], as well as typical ξ values (30-60 fJ/V-m) measured in the Ta|CoFeB|MgO system.[26,28,42-44] The results also show that a higher annealing temperature improves the M_S, as well as the interfacial PMA K_i of the film stack within the studied temperature range. *Ab initio* electronic structure calculation results further show that the calculated K_i values increase as the epitaxial tensile strain on the FeCo layers relaxes. In addition, the CoFeB thickness dependences of the VCMA and K_i are studied in this work for annealing at different temperatures, showing no significant dependences over the measured thickness range.

2.2 Measurement and methods

The magnetic film stacks were deposited in a magnetron sputtering system on a thermally oxidized Si|SiO$_2$ substrate. We prepared samples with a uniform CoFeB thickness with the following structures: Mo(5)|Co$_{20}$Fe$_{60}$B$_{20}$(t=0.94,1.06,1.18)|MgO(2.5)|Al$_2$O$_3$(5), with the numbers in the parentheses designating nominal thickness in nm. We also deposited samples with gradually changing (wedged) CoFeB thickness with similar structures: Mo(5)|Co$_{20}$Fe$_{60}$B$_{20}$(t)|MgO(2.5)|Al$_2$O$_3$(5), where the CoFeB thickness t was continuously varied in the range of 0.65 to 1.45 nm across the wafer. All metallic layers were grown using DC sputtering, while the MgO and Al$_2$O$_3$ layers were RF sputtered from insulating MgO and Al$_2$O$_3$ targets. Stacks were annealed at 360°C, 400°C, and 430°C respectively for 30 minutes under vacuum (< 10^{-7} Torr). The rise time of the annealing system was less than 2 minutes, while the cool-down time from 430°C to 200°C was approximately 30 minutes. The samples were subsequently patterned into Hall bar devices by standard photolithography and dry etching techniques, and further covered by a 33 nm Al$_2$O$_3$ gate oxide using atomic layer deposition (ALD).

9

Last, a patterned ITO electrode was fabricated on top for gating. The dielectric constants of MgO and Al_2O_3 are assumed to be 10 and 7, respectively according to the literature, for the calculation of the electric field strength at the CoFeB|MgO interface.[45,46] The dimensions of the Hall bars were $20 \, \mu m \times 130 \, \mu m$. For the wedged samples, the Hall bar length was perpendicular to the wedge direction.

Ab initio electronic structure calculations were carried out within the framework of the projector augmented-wave formalism, as implemented in the Vienna *ab initio* simulation package (VASP)[47] at the generalized gradient approximation level.[48] The slab supercell model of the magnetic layered structure consists of three monolayers (MLs) of bcc Mo, on top of 3 MLs of *B*2-type FeCo, on top of 7 MLs of MgO and a 15-Å-thick vacuum region, as shown in the inset of Figure 7 (c). The O atoms at the interface are placed atop Fe atoms.

2.3 Dependence of saturation magnetization and dead layer on annealing temperature

The unpatterned films were first characterized by a vibrating sample magnetometer (VSM) to obtain M-H loops, in order to study the change of PMA and M_S with different annealing temperatures. Exemplary results from a sample with a uniform CoFeB thickness of 1.06 nm are shown in *Figure 3*(a), where the magnetic field is swept in the out-of-plane direction. As the annealing temperature increases, the squareness of the M-H loop improves, and the out-of-plane saturation field decreases, both of which indicate that the PMA of the film increases at higher annealing temperature. Similar results were also observed for samples with CoFeB thicknesses of 0.94 and 1.18 nm. By carrying out a linear fit of the magnetic moment per unit area as a function of the CoFeB thickness, we further obtained the saturation magnetization (M_S) and dead layer

10

thickness (t_d) values at different annealing temperatures.[21] As shown in *Figure 3*(b), both the M_S and t_d values increase at higher annealing temperatures. Note that all CoFeB thicknesses mentioned in the paper refer to the nominal thickness without dead layer subtraction.
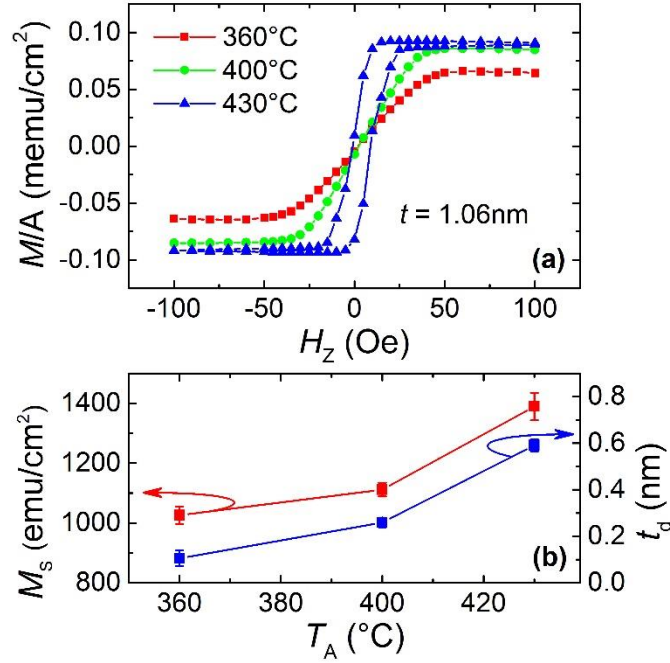
Figure 3. (a) M-H curves for different annealing temperatures (T_A). M/A refers to magnetic moment per unit area. H_Z refers to out-of-plane magnetic field. The CoFeB thickness (t) is 1.06nm. (b) Dependence of saturation magnetization (M_S) and dead layer thickness (t_d) on T_A.

This increase of PMA, M_S, and t_d in the Mo|CoFeB|MgO system with annealing temperature is consistent with the observations of Ref. [21], and can be associated with the competition between boron diffusion from the CoFeB layer into the molybdenum film,[49] and molybdenum diffusion into the CoFeB layer upon annealing. It is known that the diffusion of boron promotes better crystallization of CoFe from the amorphous state to a bcc(001) crystal structure,[50] resulting in a higher saturation magnetization. According to *ab initio* calculations, the PMA in the CoFeB|MgO system stems primarily from the hybridized Fe/Co *3d* orbitals and O *2p* orbitals at

the interface,[15,16] hence the decrease of boron atoms at the interface might be expected to induce stronger orbital hybridization and a higher PMA.

It is worth noting that the observed monotonic increase of both M_S and PMA from 360°C to 430°C in the Mo-based system is in sharp contrast to the Ta-based system, where both M_S and PMA drop when annealed at temperatures higher than 300°C.[33,49] Similarly, the dead layer thickness of the Ta|CoFeB|MgO system increases above 0.5 nm at around 330°C[21] while the dead layer thickness increases above 0.5 nm at a higher temperature of around 430°C of the Mo|CoFeB|MgO system. This better thermal annealing stability of PMA and M_S in Mo|CoFeB|MgO structures can be explained by a number of causes. Namely, the smaller negative formation enthalpy of Mo oxides compared to Ta oxides, the crystalline structure of the sputtered Mo film,[21] and the smaller negative formation energy of Fe-Mo alloys compared to Fe-Ta,[22] all contribute to the prevention of molybdenum atoms from significantly diffusing into the free layer, leading to a more stable PMA and M_S after high-temperature annealing. On the contrast, the decrease of M_S in the Ta-based system at higher annealing temperatures has been attributed to intermixing of CoFeB and Ta,[51] while the decrease of PMA results mainly from the diffusion of Ta into the CoFeB|MgO interface.[52] Hence in our Mo|CoFeB|MgO system, as the magnetic properties keep improving from 360°C to 430°C, boron diffusion (out of the free layer) has a dominating effect over molybdenum diffusion (into the free layer) over the studied temperature range.

2.4 Dependence of VCMA and interfacial PMA on annealing temperature

The VCMA was subsequently characterized as follows. The Hall resistance R_{Hall} was measured under a sweeping out-of-plane magnetic field while different gate voltages were applied.

12

A positive gate voltage is defined as the top gate electrode being at a positive electric potential, as shown in *Figure 4* top right inset. *Figure 4* shows the measurement results of the wedged sample with a CoFeB thickness of 1.45nm, annealed at 430°C for 30 minutes, where three different gate voltages are applied. As the CoFeB in this case has an in-plane easy-axis, an out-of-plane (i.e. hard-axis) magnetic field is applied in order to obtain the perpendicular anisotropy energy (E_{perp}).[26] As can be seen from the bottom left inset of *Figure 4*, a noticeable difference of the R_{Hall}-H loop is observed for different applied electric fields.
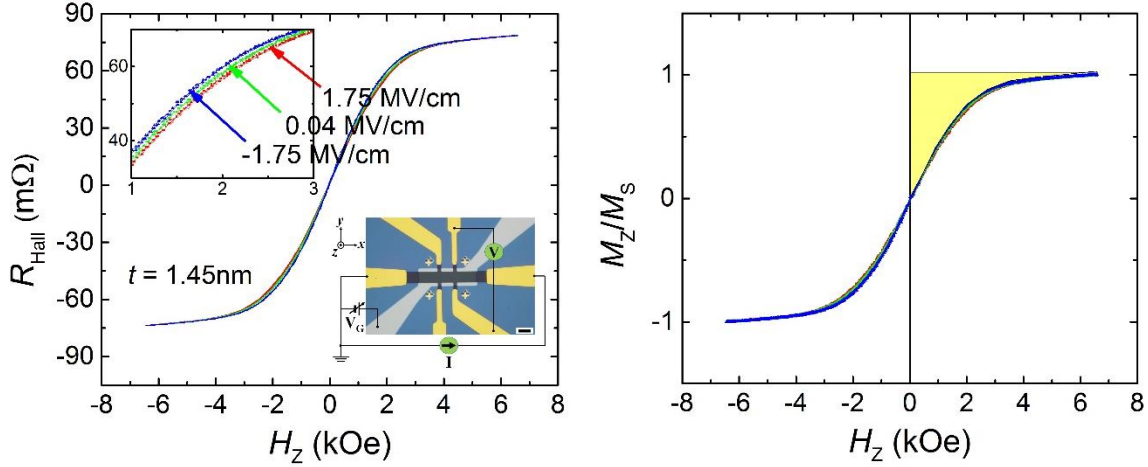
Figure 4. (Left) Hall resistance dependence on out-of-plane magnetic field, under different gate voltages. The film stack was annealed at 430°C for 30 minutes. Top right inset: Top view of a Hall bar device with an ITO gate electrode. The scale bar is $20\ \mu m$. Bottom left inset: Zoomed-in view of the main figure with the same units for both axes. (Right) Normalized Hall resistance dependence on out-of-plane magnetic field. The yellow-colored regions refers to the value of $-E_{perp}/M_S = \int_0^1 H_Z dM_Z/M_S$.

To measure the VCMA coefficient ξ, we follow an approach similar to Ref.[26]. The value of E_{perp} is obtained from the equation $E_{\text{perp}} = -M_S \int_0^1 H_Z d[2(R^{\text{AHE}} - R_{\min}^{\text{AHE}})/(R_{\max}^{\text{AHE}} - R_{\min}^{\text{AHE}}) - 1]$, where $[2(R^{\text{AHE}} - R_{\min}^{\text{AHE}})/(R_{\max}^{\text{AHE}} - R_{\min}^{\text{AHE}}) - 1]$ equals the normalized M_Z/M_S value. The value of $-E_{perp}/M_S = \int_0^1 H_Z dM_Z/M_S$ is also shown in the right figure of Figure *4*. Here, M_S is

the saturation magnetization, M_Z is the perpendicular component of the magnetization, H_Z is the out-of-plane external magnetic field, R^{AHE} is the anomalous Hall resistance, and R_{max}^{AHE} (R_{min}^{AHE}) is the maximum (minimum) of R^{AHE} values measured. The value of R^{AHE} can be extracted from R_{Hall} by subtraction of the ordinary Hall contributions according to $R_{Hall} = R_0 \mu_0 H/(t - t_d) + R_S M_Z/(t - t_d)$, where the first term is the ordinary Hall resistance, and the second term represents R^{AHE}. Here, R_0 and R_S are the ordinary and anomalous Hall coefficients, respectively, and μ_0 is the permeability of free space. The ordinary Hall coefficients can be obtained from a fit to the $R_{Hall} - H_Z$ loop at the high field regions. From this, we can obtain the electric field dependence of the perpendicular anisotropy energy $E_{perp}(E)$, and hence the electric field dependent interfacial perpendicular anisotropy (K_i) can be calculated using $E_{perp}(E) = K_i(E)/(t - t_d) - 2\pi M_S^2$. Hence, one can obtain the electric field dependence of K_i and measure the VCMA coefficient ξ.
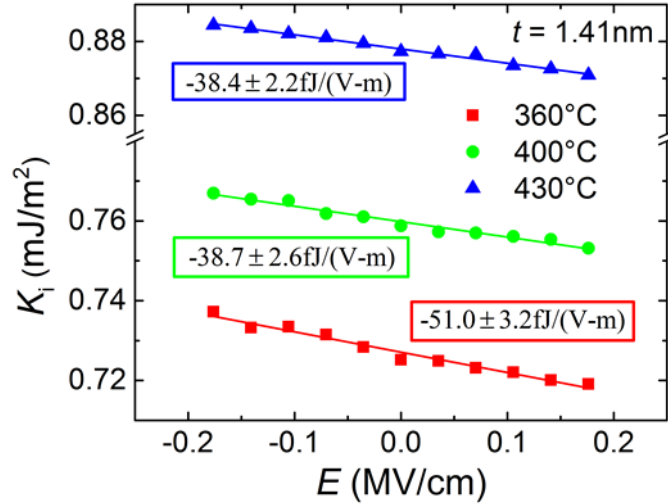
Figure 5. Interfacial perpendicular magnetic anisotropy (K_i) dependence on electric field (E) for different T_A. The inset numbers indicate the VCMA coefficient (ξ).

Next, we compare three exemplary dependencies of K_i as a function of electric field, for devices with the same CoFeB thickness annealed at different temperatures. As shown in *Figure 5*, a linear dependence with a negative slope is obtained, which means that depletion of electrons at the CoFeB|MgO interface increases the interfacial perpendicular anisotropy. From the fitted curves, a ξ of ~40 fJ/V-m is demonstrated after annealing at 430°C, along with a higher ξ of ~50 fJ/V-m at 360°C annealing temperature.
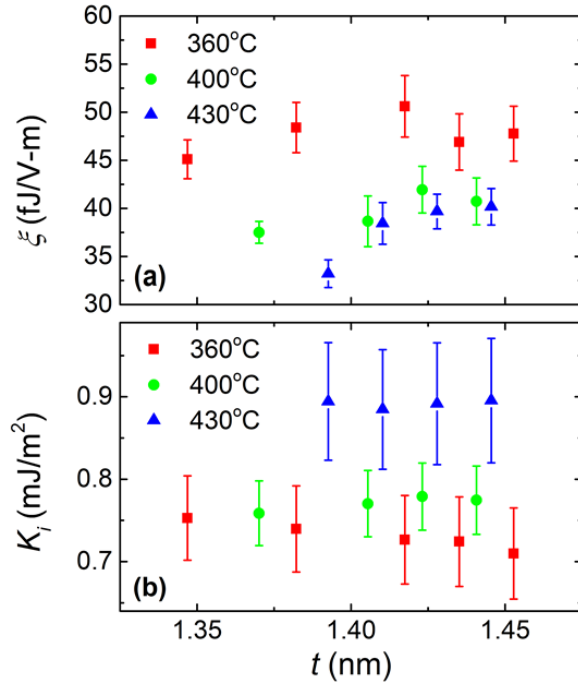
Figure 6. (a) VCMA coefficient ξ, and (b) Interfacial PMA K_i dependence on CoFeB thickness (t), under different T_A.

In addition, we carried out gate voltage-dependent hard-axis $R_{Hall} - H$ measurements for devices along the length of the wedge-shaped sample, to study the CoFeB thickness dependence of the VCMA coefficient (ξ) and interfacial perpendicular anisotropy (K_i) for different annealing temperatures, as shown in Figure 6(a) and (b). No significant CoFeB thickness dependence of either

ξ or K_i is observed over the measured thickness range, which is consistent with some previous reports,[44] that the interfacial anisotropy and its electric field control originate primarily from the CoFeB interfaces.
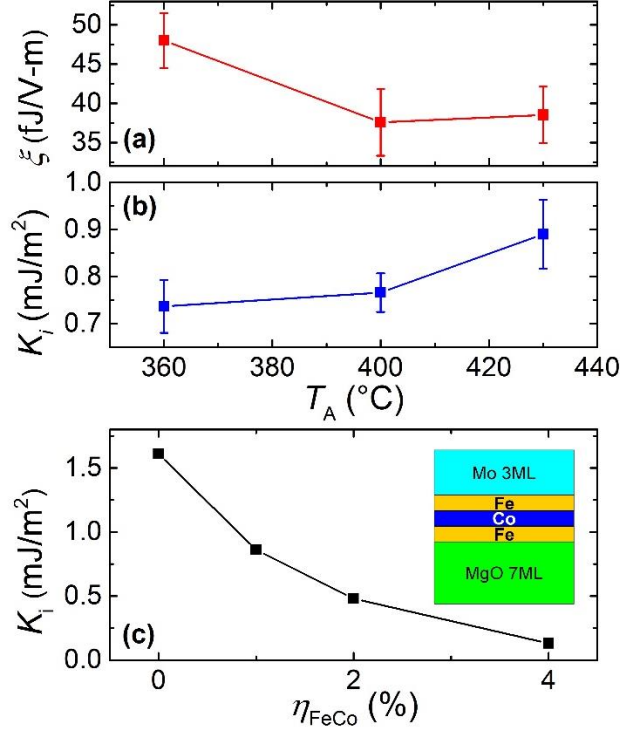
Figure 7. (a) ξ, and (b) K_i dependence on T_A. The VCMA coefficients here are all absolute values, while the measured values are all negative (according to the definition that a positive voltage corresponds to higher electric potential at the top gate electrode). Error bars are included to take into account the uncertainty in t_d and M_S values. (c) The *ab initio* electronic structure calculated K_i of Mo(3ML)|FeCo(3ML)|MgO(7ML) as a function of tensile strain on FeCo layer (η_{FeCo}).

The dependences of ξ and K_i (after averaging over the measured thickness values) on the annealing temperature are summarized in Figure 7(a) and (b). Apart from the slight decrease of the VCMA coefficient, K_i increases by 20% from 0.74 mJ/m^2 to 0.89 mJ/m^2 after annealing. This slight drop of ξ along with a continued increase of K_i at higher annealing temperature is consistent with

16

previous reports in Ir|CoFeB|MgO[25] and W|CoFeB|MgO systems[24] which indicates that the electric-field control of K_i is more sensitive to annealing effects than K_i itself. A possible reason for the increase of K_i and slight VCMA degradation at higher annealing temperature is that the annealing relaxes the compressive strain of the MgO layer, such that the lattice constant of the MgO approaches its bulk value.[53]

To further investigate the effect of strain on K_i, Dr. P. V. Ong and Professor Nicholas Kioussis in the Department of Physics and Astronomy at California State University Northridge performed *ab initio* electronic structure calculations of interfacial PMA (K_i) in Mo(3ML)|FeCo(3ML)|MgO(7ML) structures, as a function of tensile strain on the FeCo layer (η_{FeCo}). As shown in Figure 7(c), the relaxation of epitaxial FeCo strain, thus relaxation of epitaxial MgO strain, can give rise to an increase of K_i. Note that as discussed before, the diffusion of boron atoms away from the CoFeB|MgO interface might also contribute to the increase of interfacial PMA. According to our recent *ab initio* work on the dependence of VCMA on epitaxial strain of CoFeB|MgO structures, a relaxation of compressive strain of the MgO layer will lead to a lower dielectric constant of the MgO, which might reduce the VCMA effect.[54]

2.5 Discussion and conclusion

It is worthwhile to compare our results to those obtained in other material systems of interest for MeRAM. Thermal stability of VCMA above 400°C has been previously studied in the W|CoFeB|MgO system.[24] Our observed ξ values, along with a slight decrease of the ξ values above 400°C in the Mo-based system, are very similar to those in the W-based system. The comparable ξ values between the two material systems also agree well with a previous experiment on vacuum|Fe|Mo(110) and vacuum|Fe|W(110) systems using nanoscale ferromagnetic islands on

metallic substrates at 45 K.[29] While for Ta|CoFeB|MgO structures, a VCMA coefficient of 30-60fJ/V-m has been obtained in several previous work with annealing temperatures below 300°C.[26,28,42-44] In other structures with seed layers such as Au,[10] Ru,[28] Ir,[25] Ag, CuN, Zr, Nb,[24] and MgO,[55] ξ values of 20-100fJ/V-m have been demonstrated with annealing temperatures generally not exceeding 350°C.

It is also worth noting that a number of reports have shown large ξ values of 100-1,200fJ/V-m,[56-58] which can be attributed to mobile ionic charges in the oxides besides the MgO layer. These charges may, however, be too slow to achieve high frequency memory writing using voltage pulses. To eliminate the possibility of such an ionic effect in our films, we carried out a hysteretic sweep of the gate voltage[56] from -10V to 10V and back to -10V. The K_i vs electric field plots for different sweeping directions coincide with each other and are within the error bars of the measurement, hence confirming that there is no contribution from mobile charges in our films.

In conclusion, it is demonstrated that the interfacial PMA in Mo|CoFeB|MgO structures increases and the VCMA is sustained with annealing temperatures up to 430°C. A VCMA coefficient of 40 fJ/V-m is demonstrated after annealing at 430°C, indicating a VCMA comparable to Ta-seeded systems, along with a marked improvement in its temperature stability. *Ab initio* electronic structure calculations further corroborate the enhancement of experimental K_i values at high temperatures. No significant CoFeB dependence of the VCMA effect and the interfacial PMA is observed over the thickness range studied. The demonstration of thermally stable VCMA and PMA provides a pathway for the integration of Mo|CoFeB|MgO into Magnetoelectric RAM devices compatible with advanced embedded CMOS technologies.

Chapter 3: Dependence of Voltage-controlled Magnetic Anisotropy on Ferromagnetic Layer Thickness in Perpendicular Ta|CoFeB|MgO-based Structures

3.1 Motivation

For practical memory applications where the free layer CoFeB thickness t_{CoFeB} can be tuned to achieve optimal PMA, TMR, and thermal stability,[20,59,60] it is important to investigate the effect of t_{CoFeB} on the VCMA. There have been few studies on the t_{CoFeB} dependent VCMA effect: one obtained an almost constant VCMA effect of 60 fJ/V-m for varying t_{CoFeB} using angle-dependent ferromagnetic resonance (FMR) technique in a microwave cavity,[44] while several others investigated the effect of electric field on perpendicular CoFeB coercivities for different t_{CoFeB}.[9,61] Though coercivity is correlated with saturation field, it is more accurate to quantify the VCMA effect in terms of interfacial PMA change per unit electric field. Hence, an accurate study on the CoFeB thickness dependent VCMA effect using transport measurements is critical.

Existing DC transport methods to achieve this goal mainly include two. One is anomalous Hall resistance measurement in CoFeB|MgO|oxide structures with an applied gate voltage, hereafter referred to as anomalous Hall measurement,[26]. The other is MTJ resistance measurement using a free layer and a fixed layer with specific magnetization configurations. The most accurate configuration to extract the VCMA coefficient is one where the fixed layer does not change its magnetization orientation when a hard-axis loop for the free layer is swept, hereafter referred to as strong fixed layer MTJ measurement.[42,43] However, this scenario is rather difficult to achieve as a synthetic antiferromagnetic (SAF) structure is usually required for the strong pinning of the fixed layer. Henceforth, another special configuration that deviates from the abovementioned ideal

scenario is often adopted which uses a weak in-plane layer that switches at a rather low in-plane magnetic field,[28,55,62] hereafter referred to as weak reference layer MTJ measurement. In this scenario, the free layer has been assumed to be fully perpendicular at zero external magnetic field and fully in-plane at maximum in-plane external field. Here we explore these different methods and evaluate the validity of the different assumptions used to quantify the VCMA strength, looking especially at the anomalous Hall and weak reference layer MTJ measurements methods.

In this section, we utilize both anomalous Hall and weak reference layer MTJ measurements to obtain the VCMA coefficient for Ta|CoFeB|MgO-based structures with different CoFeB thicknesses, where the CoFeB layer is thin enough to exhibit a perpendicular easy-axis. Hard-axis R-H loops under different applied voltages are performed to extract the change of the interfacial perpendicular anisotropy as function of electric field, i.e. the VCMA coefficient. To obtain the interfacial PMA value under one specific applied electric field, the R-H loop under this applied electric field has to be normalized into an M-H loop. In this normalization process, one has to determine at least two anomalous Hall and/or MTJ resistance ($R_{\text{Hall}}/R_{\text{MTJ}}$) values under each applied electric field to be referenced to specific perpendicular component of magnetization (M_{Z}) values (e.g. $M_{\text{Z}} = 0, \pm M_{\text{S}}$). We compare the CoFeB thickness dependent VCMA effect using two normalization methods to convert $R_{\text{Hall}}/R_{\text{MTJ}}$ values into the perpendicular component of magnetization M_{Z} in the VCMA calculations. The widely used "individual" normalization method which assumes that at zero external magnetic field the magnetization is always fully perpendicular for each individual electric field case,[28,55,62] results in a strong CoFeB thickness dependent VCMA effect. In this case, the reference values of $R_{\text{Hall}}/R_{\text{MTJ}}$ are determined to be different for each applied electric field. However, if an

"overall" normalization method considering that the anomalous Hall resistance (thus perpendicular component of magnetization) values at zero magnetic field change under different electric fields, an almost constant VCMA dependence on CoFeB thickness over the studied range is obtained. In this case, the same reference value of R_{Hall} for different applied electric field cases is used. In addition, the drop of VCMA coefficient at perpendicular to in-plane CoFeB transition thickness is also discussed, which can be explained by the multi-domain behavior of the CoFeB layer.

3.2 Materials and methods

CoFeB with gradually changing (wedged) thickness were deposited as part of stacks grown on a thermally oxidized Si/SiO$_2$ substrate in a magnetron sputtering system to study the t_{CoFeB} dependence of the VCMA effect. The stack used in the weak reference layer MTJ measurement was Ta(18)|Co$_{20}$Fe$_{60}$B$_{20}$(t_{CoFeB})|MgO(2.5)|Co$_{20}$Fe$_{60}$B$_{20}$(2)|Ta(4)|Pt (2), (thickness in nm), consisting of a wedged CoFeB free layer and a 2 nm-thick weak CoFeB reference layer. The stack for the anomalous Hall measurement was Ta(5)|Co$_{20}$Fe$_{60}$B$_{20}$(t_{CoFeB})|MgO(2.5)|Al$_2$O$_3$ (5). The wedged CoFeB layer thickness t_{CoFeB} is continuously varied in the range of 0.7 to 1.4 nm across the wafer in both stacks. All metallic layers were deposited using DC sputtering, while the MgO and Al$_2$O$_3$ layers were deposited using RF sputtering from insulating MgO and Al$_2$O$_3$ targets. All stacks were annealed at 250°C for 30 minutes in a vacuum under 10^{-7} Torr, and then measured by a superconducting quantum interference device (SQUID) to obtain saturation magnetization values, which are 841 emu/cm^3 and 999 emu/cm^3 for stacks used in the MTJ and anomalous Hall measurement, respectively.

The stack for MTJ measurement was fabricated into MTJs with the elliptical diameters of

21

$4\ \mu m \times 8\ \mu m$ using standard photolithography and reactive ion etching (RIE) techniques. The stack for anomalous Hall measurement was patterned into Hall bar devices, which were further covered by a 33 nm thick Al_2O_3 gate oxide, deposited by atomic layer deposition (ALD) at 200°C for 30 minutes. Next, a patterned ITO electrode was fabricated for top gating. The dielectric constants of MgO and Al_2O_3 are assumed to be 10 and 7 respectively for the calculation of the electric field strength at the CoFeB|MgO interface.[45,46] The dimensions of the Hall bar were $20\ \mu m \times 130\ \mu m$ and the Hall bar length was perpendicular to the wedge direction.

3.3 Weak reference layer MTJ measurement

We first used the MTJ structure with a weak in-plane fixed layer and a perpendicular free layer. The MTJ resistance was measured under a varying in-plane magnetic field while bias voltages were varied. The positive bias voltage is defined as the top electrode is at a positive electric potential.

Using a similar method as used in Ref. [28], the perpendicular anisotropy energy E_{perp} can be obtained using the following equation $E_{\text{perp}} = M_S \int_0^1 H_X\, d(M_X/M_S)$, where the normalized in-plane magnetization component $M_X/M_S = [G(H_X, E) - G(0, E)]/[G(H_X^{\max}, E) - G(0, E)]$. Here, M_S is the saturation magnetization, M_X is the in-plane component of magnetization, $G(H_X, E)$ is the MTJ conductance at an in-plane magnetic field H_X and electric field E, while $G(0, E)\ [G(H_x^{\max}, E)]$ is the conductance at zero [maximum] in-plane field and electric field E, which acts as the reference value in the normalization process. Then the interfacial magnetic anisotropy K_i can be obtained by $K_i = (2\pi M_S^2 + E_{\text{perp}})t_{\text{CoFeB}}$.[20] By applying different bias voltages, VCMA coefficient ξ can be calculated by linear fitting K_i as a function of E. The *R-H*

loops for a MTJ with 0.91nm CoFeB free layer under different E are shown in *Figure 8*(a). The lower MTJ resistance at higher bias voltages is due to the inherent bias dependence of the TMR effect.
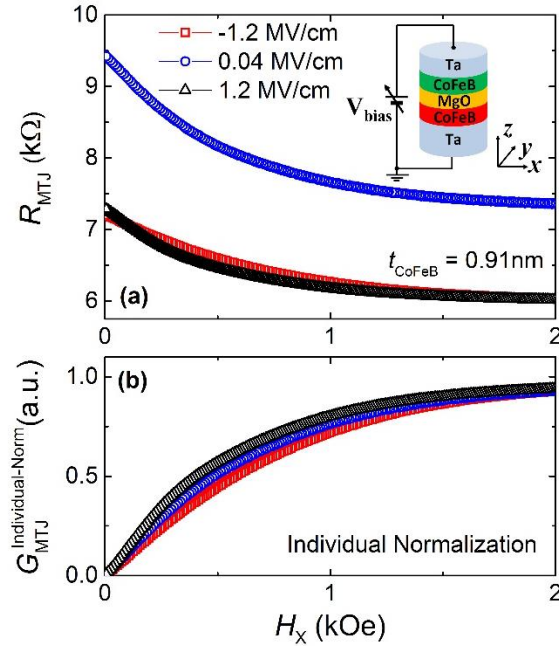
Figure 8. (a) Magnetic tunnel junction (MTJ) resistance R_{MTJ} versus external in-plane magnetic field H_X curves for different applied bias electric fields. The inset shows the schematic for the MTJ with varied bias voltage V_{bias} applied. (b) Individual-normalized MTJ conductance $G_{MTJ}^{Individual-Norm}$, which takes the maximum conductance range of each $G_{MTJ} - H_X$ loop as reference for normalization.

Note that this method is only valid if the magnetization of the free layer is fully perpendicular under zero external magnetic field for all CoFeB thicknesses and all applied electric fields. As the normalization process that calculates M_X/M_S is carried out for conductance values at each individual measured electric field, we refer to the M_X/M_S value as the individual-normalized MTJ conductance $G_{MTJ}^{Individual-Norm}$, as shown in *Figure 8*(b).

3.4 Anomalous Hall measurement

The VCMA effect was also studied by measuring the Hall resistance R_{Hall} under a varying in-plane magnetic field H_X, with different applied gate voltages. The positive gate voltage is defined as the top gate electrode being at a positive electric potential similar as in the previous sections. The electric-field dependent R-H loops for a perpendicular Hall bar device with $t_{\text{CoFeB}} = 0.8\text{nm}$ is shown in *Figure 9*(a). The switching behavior is due to the small misalignment of the device plane with respect to the in-plane magnetic field direction.

To quantitatively measure the VCMA coefficient ξ, we utilized a similar method as Ref.[26]. Note that here the CoFeB film is perpendicular easy axis, hence we have to apply an in-plane hard axis loop to characterize the perpendicular anisotropy. While in the previous chapter, an out-of-plane magnetic field is applied for the in-plane easy axis film. First, we obtain the $E_{\text{perp}} = M_S \int_0^1 H_X d(M_X/M_S)$, where $M_X/M_S = \sqrt{1 - (M_Z/M_S)^2}$, the normalized perpendicular magnetization component $M_Z/M_S = 2(R_{\text{AHE}} - R_{\text{min}}^{\text{AHE}})/(R_{\text{max}}^{\text{AHE}} - R_{\text{min}}^{\text{AHE}}) - 1$. Here, M_Z is the perpendicular component of the magnetization, and $R_{\text{max}}^{\text{AHE}}$ ($R_{\text{min}}^{\text{AHE}}$) is the maximum (minimum) of R_{AHE} values. Note that as the external in-plane field has a very small misalignment angle (determined to be less than 0.05 rad) with respect to the device plane, the ordinary Hall Effect contribution to the total Hall resistance is negligible. Hence, R_{Hall} can be safely assumed to be the same as the anomalous Hall resistance R_{AHE}, thus proportional to M_Z. Similar to the weak reference layer MTJ measurement described previously, the VCMA coefficient is calculated by linearly fitting K_i as a function of E.

One caveat in the above mentioned calculations is the choice of $R_{\text{max}}^{\text{AHE}}$ and $R_{\text{min}}^{\text{AHE}}$ values for

each applied electric field case. One method similar to the individual normalization method used in the MTJ measurement is to calculate $M_Z/M_S =$

$$2[R_{AHE}(E) - R_{min}^{AHE}(E)]/[R_{max}^{AHE}(E) - R_{min}^{AHE}(E)] - 1$$

for every individual electric field E. We will refer to the M_Z/M_S value obtained in the way as the individual-normalized Hall resistance $R_{Hall}^{Individual-Norm}$, as shown in *Figure 9*(c). It is thus expected that the $R_{Hall}^{Individual-Norm}$ values will have a value of one at zero external field. This means that the magnetization at $H_X = 0$ is fully perpendicular under all electric fields, which is the same assumption used in the weak reference layer MTJ method.
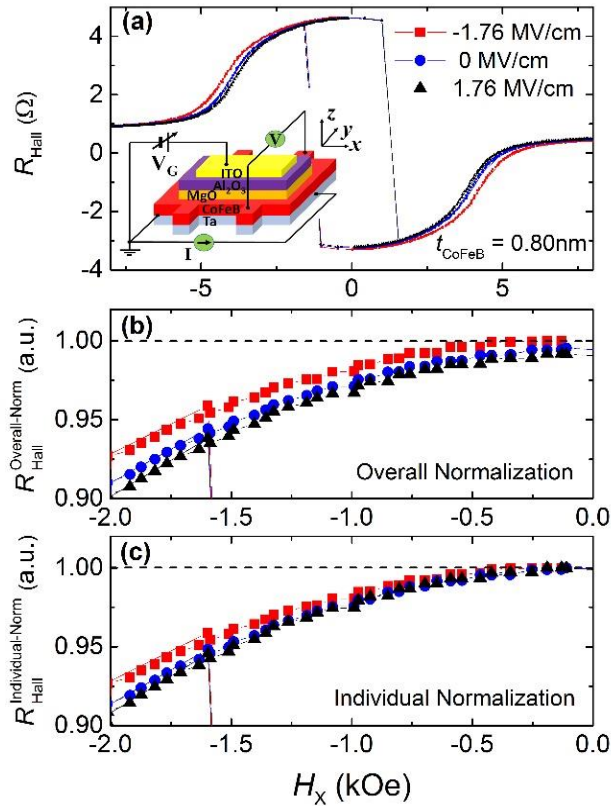

Figure 9. (a) Hall resistance R_{Hall} versus H_X curves for different applied electric fields. The inset shows the schematic for the Hall bar device with varied gate voltage V_G, (b) Overall-normalized Hall resistance

$R_{Hall}^{Overall-Norm}$, which takes the maximum conductance range of each $G_{MTJ} - H_X$ loop as reference for normalization. (c) Individual-normalized Hall resistance $R_{Hall}^{Individual-Norm}$, which takes the maximum resistance range of each $R_{Hall} - H_X$ loop at one specific electric field as reference for normalization.

However, as the Hall resistance is directly proportional to the M_Z, after careful inspection of *Figure 9*(a), the zero-field R or R_{max}^{AHE} changes with different electric fields. This clearly indicates that the free layer magnetization does not stay fully perpendicular when varied electric fields are applied. If we take the maximum $\left(R_{max}^{AHE} - R_{min}^{AHE}\right)$ value across all electric field cases (E_0= -1.76 MV/cm in this experiment) in the normalization to obtain the M_Z/M_S value, which will be referred to as the overall normalization method hereafter, we can obtain the overall normalized Hall resistance $R_{Hall}^{Overall-Norm}$ as $M_Z/M_S = 2[R^{AHE}(E) - R_{min}^{AHE}(E_0)]/[R_{max}^{AHE}(E_0) - R_{min}^{AHE}(E_0)] - 1$, as shown in *Figure 9*(b). The M_Z/M_S value decreases under positive electric field, which is consistent with the decrease of calculated E_{perp} at positive electric field, both corresponding to a negative VCMA coefficient ξ.

3.5 VCMA based on different normalization methods

As discussed, we used the individual normalization method for the MTJ measurement, and both individual and overall normalization methods for the anomalous Hall measurement. The obtained magnitude of VCMA coefficient as a function of CoFeB thickness is shown in *Figure 10*(a). Note that all measured VCMA coefficients are negative according to our definition that a higher electric potential at the top electrode (opposite to the substrate) corresponds to positive electric field.

It can be seen that the individual normalization method results in a similar strong VCMA dependence on the CoFeB thickness for both Hall and MTJ measurements, where the ξ values

both peak at $t_{CoFeB} \sim 0.9$nm. While the overall normalization method gives rise to a weak VCMA

dependence on the CoFeB thickness when 0.8nm $< t_{CoFeB} < 0.95$nm.
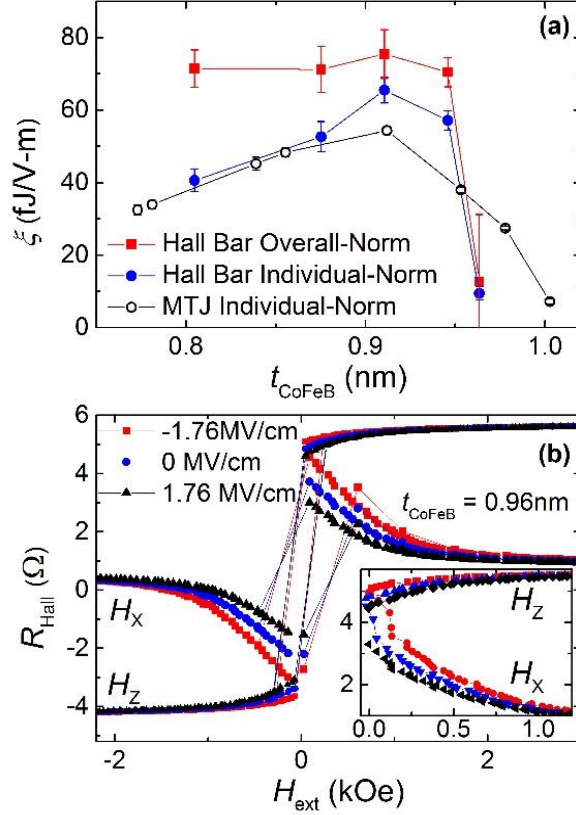
Figure 10. (a) VCMA coefficient ξ dependence on the CoFeB thickness t_{CoFeB}, obtained from the overall and individual normalized Hall bar R-H data, and individual normalized MTJ R-H data. (b) Hall resistance R_{Hall} versus external in-plane (out-of-plane) magnetic field $H_X(H_Z)$ curve for different applied electric fields. The inset shows the zoomed-in region with positive external magnetic field.

3.6 Discussion and conclusion

According to the decrease of R_{max}^{AHE} at positive electric fields, as indicated from *Figure 9*(b), we can conclude that at zero external magnetic field ($H_X = 0$), the perpendicular component of magnetization (M_Z) changes under different electric fields in the Hall bar device. Thus it is more

accurate to use the overall normalization method to calculate the VCMA coefficient for the anomalous Hall measurement. However, as both TMR and MTJ resistance at $H_X = 0$ depend on the bias voltage,[17,59] it is very difficult to determine the actual M_Z values at $H_X = 0$ under different electric fields using the weak reference layer MTJ measurement method alone.

Using the overall normalization method, the obtained ξ value of around 70 fJ/V-m is at the upper bound of previous reported ξ values ranging from 30 to70 fJ/V-m.[26,28,42-44,63] The obtained weak VCMA dependence on the CoFeB thickness over the studied range is also consistent with previous work,[44] which indicates the interfacial origin of VCMA effect from the CoFeB/MgO interface.

On the other hand, the individual normalization method underestimates the VCMA coefficients and results in an artificial strong VCMA dependence on the CoFeB thickness due to an error in converting the MTJ/anomalous Hall resistance into the magnetization values. The fact that the ξ peaks at $t_{CoFeB} \sim 0.9$nm for both Hall and MTJ measurements using an individual normalization method also indicates that the M_Z value for the free layer in the weak reference layer MTJ is not constant under different bias voltages. Nevertheless, we expect that VCMA measurements using a strong-fixed layer MTJ should not suffer from this problem.

To explain the sharp decrease of VCMA with $t_{CoFeB} > 0.95$nm, we carried out both in-plane and out-of-plane R-H loops using the anomalous Hall measurement. As can be seen in the in-plane loops in *Figure 10*(b), at $H_X = 0$, the Hall resistance decreases significantly from negative to positive electric field (more than 30%). In contrast, the Hall resistance change under electric field at $t_{CoFeB} < 0.95$ nm range is very small (less than 2%), as shown in *Figure 9*(a) and (b). The out-of-plane loops further validates that the magnetization is not fully perpendicular at $H_Z = 0$,

and R^{AHE} decreases significantly at positive electric field (more than 10%).

More importantly, the Hall resistance at zero external magnetic field for a single electric field, but with different external magnetic field directions (H_X or $H_Z = 0$), do not coincide with each other. This means that the free layer breaks into multi-domain configurations, which will contribute to the reduction of the E_{perp} in addition to the external magnetic field contribution. Thus, the VCMA coefficient calculated will be significantly smaller than the real VCMA value. This can also explain the decrease of VCMA obtained by the MTJ measurement at $t_{CoFeB} > 0.95$ nm.

Two normalization methods were used to measure the VCMA effect in Hall bar and MTJ devices. It was shown that in order to obtain accurate VCMA coefficients, the overall normalization method should be used where the change of the perpendicular component of magnetization at zero external magnetic field under different electric fields is considered. In contrary, the MTJ measurement using a weak in-plane fixed layer that switches at low in-plane field will result in artificially lowered VCMA coefficients.

Using the overall normalization method, we obtained rather constant VCMA coefficients of around 70 fJ/V-m for perpendicular CoFeB with thicknesses ranging from 0.8nm to 0.95nm. Whereas for CoFeB with thickness above 0.95nm, the multi-domain behavior will result in a sharp decrease of measured VCMA coefficients.

References

[1] K. L. Wang, J. G. Alzate, and P. Khalili Amiri, Journal of Physics D: Applied Physics **46** (7), 074003 (2013).

[2] K. Lee and S. H. Kang, Ieee T Magn **47** (1), 131 (2011).

[3] J. C. Slonczewski, Journal of Magnetism and Magnetic Materials **159** (1-2), L1 (1996).

[4] E. B. Myers, D. C. Ralph, J. A. Katine, R. N. Louie, and R. A. Buhrman, Science **285** (5429), 867 (1999).

[5] I. M. Miron, K. Garello, G. Gaudin, P. J. Zermatten, M. V. Costache, S. Auffret, S. Bandiera, B. Rodmacq, A. Schuhl, and P. Gambardella, Nature **476** (7359), 189 (2011).

[6] Luqiao Liu, O. J. Lee, T. J. Gudmundsen, D. C. Ralph, and R. A. Buhrman, Physical Review Letters **109** (9), 096602 (2012).

[7] P. Khalili and K. L. Wang, Ieee Spectrum **52** (7), 30 (2015).

[8] R. Dorrance, J. G. Alzate, S. S. Cherepov, P. Upadhyaya, I. N. Krivorotov, J. A. Katine, J. Langer, K. L. Wang, P. K. Amiri, and D. Markovic, Electron Device Letters, IEEE **34** (6), 753 (2013).

[9] W. G. Wang, M. Li, S. Hageman, and C. L. Chien, Nat Mater **11** (1), 64 (2012).

[10] Y. Shiota, T. Nozaki, F. Bonell, S. Murakami, T. Shinjo, and Y. Suzuki, Nat Mater **11** (1), 39 (2012).

[11] J. G. Alzate, P. K. Amiri, P. Upadhyaya, S. S. Cherepov, J. Zhu, M. Lewis, R. Dorrance, J. A. Katine, J. Langer, K. Galatsis, D. Markovic, I. Krivorotov, and K. L. Wang, Electron Devices Meeting (IEDM), 2012 IEEE International, 29.5.1 (2012).

[12] S. Kanai, M. Yamanouchi, S. Ikeda, Y. Nakatani, F. Matsukura, and H. Ohno, Applied Physics Letters **101** (12), 122403 (2012).

[13] KANG L. WANG and PEDRAM KHALILI AMIRI, SPIN **02** (03), 1240002 (2012).

[14] P. Khalili Amiri, J. G. Alzate, X. Q. Cai, F. Ebrahimi, Q. Hu, K. Wong, C. Grezes, H. Lee, G. Yu, X. Li, M. Akyol, Q. Shao, J. A. Katine, J. Langer, B. Ocker, and K. L. Wang, Magnetics, IEEE Transactions on **51** (11), 1 (2015).

[15] H. X. Yang, M. Chshiev, B. Dieny, J. H. Lee, A. Manchon, and K. H. Shin, Physical Review B **84** (5), 054401 (2011).

[16] K. H. He, J. S. Chen, and Y. P. Feng, Applied Physics Letters **99** (7), 072503 (2011).

[17] S. Yuasa, T. Nagahama, A. Fukushima, Y. Suzuki, and K. Ando, Nat Mater **3** (12), 868 (2004).

[18] S. S. Parkin, C. Kaiser, A. Panchula, P. M. Rice, B. Hughes, M. Samant, and S. H. Yang, Nat Mater **3** (12), 862 (2004).

[19]   P. Khalili Amiri, Z. M. Zeng, J. Langer, H. Zhao, G. Rowlands, Y. J. Chen, I. N. Krivorotov, J. P. Wang, H. W. Jiang, J. A. Katine, Y. Huai, K. Galatsis, and K. L. Wang, Applied Physics Letters **98** (11), 112507 (2011).

[20]   S. Ikeda, K. Miura, H. Yamamoto, K. Mizunuma, H. D. Gan, M. Endo, S. Kanai, J. Hayakawa, F. Matsukura, and H. Ohno, Nature Materials **9** (9), 721 (2010).

[21]   T. Liu, Y. Zhang, J. W. Cai, and H. Y. Pan, Sci Rep-Uk **4**, 5895 (2014).

[22]   H. Almasi, D. Reifsnyder Hickey, T. Newhouse-Illige, M. Xu, M. R. Rosales, S. Nahar, J. T. Held, K. A. Mkhoyan, and W. G. Wang, Applied Physics Letters **106** (18), 182406 (2015).

[23]   Gwang-Guk An, Ja-Bin Lee, Seung-Mo Yang, Jae-Hong Kim, Woo-Seong Chung, and Jin-Pyo Hong, Acta Materialia **87** (0), 259 (2015).

[24]   Witold Skowroński, Takayuki Nozaki, Duong D. Lam, Yoichi Shiota, Kay Yakushiji, Hitoshi Kubota, Akio Fukushima, Shinji Yuasa, and Yoshishige Suzuki, Physical Review B **91** (18), 184410 (2015).

[25]   Witold Skowroński, Takayuki Nozaki, Yoichi Shiota, Shingo Tamaru, Kay Yakushiji, Hitoshi Kubota, Akio Fukushima, Shinji Yuasa, and Yoshishige Suzuki, Applied Physics Express **8** (5), 053003 (2015).

[26]   M. Endo, S. Kanai, S. Ikeda, F. Matsukura, and H. Ohno, Applied Physics Letters **96** (21), 212503 (2010).

[27]   A. Rajanikanth, T. Hauet, F. Montaigne, S. Mangin, and S. Andrieu, Applied Physics Letters **103** (6), 062402 (2013).

[28]   Yoichi Shiota, Frédéric Bonell, Shinji Miwa, Norikazu Mizuochi, Teruya Shinjo, and Yoshishige Suzuki, Applied Physics Letters **103** (8), 082410 (2013).

[29]   A. Sonntag, J. Hermenau, A. Schlenhoff, J. Friedlein, S. Krause, and R. Wiesendanger, Physical Review Letters **112** (1) (2014).

[30]   K. L. Wang and P. Khalili Amiri, Spin **02** (02), 1250009 (2012).

[31]   Xiang Li, Guoqiang Yu, Hao Wu, P. V. Ong, Kin Wong, Qi Hu, Farbod Ebrahimi, Pramey Upadhyaya, Mustafa Akyol, Nicholas Kioussis, Xiufeng Han, Pedram Khalili Amiri, and Kang L. Wang, Applied Physics Letters **107** (14), 142403 (2015).

[32]   Wei-Gang Wang, Stephen Hageman, Mingen Li, Sunxiang Huang, Xiaoming Kou, Xin Fan, John Q. Xiao, and C. L. Chien, Applied Physics Letters **99** (10), 102502 (2011).

[33]   M. Yamanouchi, R. Koizumi, S. Ikeda, H. Sato, K. Mizunuma, K. Miura, H. D. Gan, F. Matsukura, and H. Ohno, Journal of Applied Physics **109** (7), 07C712 (2011).

34   K. Yamane, Y. Higo, H. Uchida, Y. Nanba, S. Sasaki, H. Ohmori, K. Bessho, and M. Hosomi, Ieee T Magn **49** (7), 4335 (2013).

35   Luc Thomas, Guenole Jan, Jian Zhu, Huanlong Liu, Yuan-Jen Lee, Son Le, Ru-Ying Tong, Keyu Pi, Yu-Jen Wang, Dongna Shen, Renren He, Jesmin Haq, Jeffrey Teng, Vinh Lam, Kenlin Huang, Tom Zhong, Terry Torng, and Po-Kang Wang, Journal of Applied Physics **115** (17), 172615 (2014).

36   J. Swerts, S. Mertens, T. Lin, S. Couet, Y. Tomczak, K. Sankaran, G. Pourtois, W. Kim, J. Meersschaut, L. Souriau, D. Radisic, S. Van Elshocht, G. Kar, and A. Furnemont, Applied Physics Letters **106** (26), 262407 (2015).

37   M. Gottwald, J. J. Kan, K. Lee, X. Zhu, C. Park, and S. H. Kang, Applied Physics Letters **106** (3), 032413 (2015).

38   T. Liu, J. W. Cai, and Li Sun, AIP Advances **2** (3), 032151 (2012).

39   D. C. Worledge, G. Hu, David W. Abraham, P. L. Trouilloud, and S. Brown, Journal of Applied Physics **115** (17), 172601 (2014).

40   B. Fang, X. Zhang, B. S. Zhang, Z. M. Zeng, and J. W. Cai, AIP Advances **5** (6), 067116 (2015).

41   Note that due to finite temperature rise and fall time of the annealing process, the actual annealing time is in fact longer.

42   Jian Zhu, J. A. Katine, Graham E. Rowlands, Yu-Jin Chen, Zheng Duan, Juan G. Alzate, Pramey Upadhyaya, Juergen Langer, Pedram Khalili Amiri, Kang L. Wang, and Ilya N. Krivorotov, Physical Review Letters **108** (19), 197203 (2012).

43   Juan G. Alzate, Pedram Khalili Amiri, Guoqiang Yu, Pramey Upadhyaya, Jordan A. Katine, Juergen Langer, Berthold Ocker, Ilya N. Krivorotov, and Kang L. Wang, Applied Physics Letters **104** (11), 112410 (2014).

44   A. Okada, S. Kanai, M. Yamanouchi, S. Ikeda, F. Matsukura, and H. Ohno, Applied Physics Letters **105** (5), 052415 (2014).

45   J. Robertson, The European Physical Journal Applied Physics **28** (3), 265 (2004).

46   M. D. Groner, J. W. Elam, F. H. Fabreguette, and S. M. George, Thin Solid Films **413** (1-2), 186 (2002).

47   G. Kresse and J. Furthmuller, Computational Materials Science **6** (1), 15 (1996).

48   J. P. Perdew, K. Burke, and M. Ernzerhof, Physical Review Letters **77** (18), 3865 (1996).

49   Jaivardhan Sinha, Maria Gruber, Masaya Kodzuka, Tadakatsu Ohkubo, Seiji Mitani, Kazuhiro Hono, and Masamitsu Hayashi, Journal of Applied Physics **117** (4), 043913 (2015).

[50] Toyoo Miyajima, Takahiro Ibusuki, Shinjiro Umehara, Masashige Sato, Shin Eguchi, Mineharu Tsukada, and Yuji Kataoka, Applied Physics Letters **94** (12), 122501 (2009).

[51] Jaivardhan Sinha, Masamitsu Hayashi, Andrew J. Kellock, Shunsuke Fukami, Michihiko Yamanouchi, Hideo Sato, Shoji Ikeda, Seiji Mitani, See-hun Yang, Stuart S. P. Parkin, and Hideo Ohno, Applied Physics Letters **102** (24), 242405 (2013).

[52] N. Miyakawa, D. C. Worledge, and K. Kita, Magnetics Letters, IEEE **4**, 1000104 (2013).

[53] S. Ikeda, J. Hayakawa, Y. Ashizawa, Y. M. Lee, K. Miura, H. Hasegawa, M. Tsunoda, F. Matsukura, and H. Ohno, Applied Physics Letters **93** (8), 082508 (2008).

[54] P. V. Ong, Nicholas Kioussis, D. Odkhuu, P. Khalili Amiri, K. L. Wang, and Gregory P. Carman, Physical Review B **92** (2), 020407 (2015).

[55] Takayuki Nozaki, Kay Yakushiji, Shingo Tamaru, Masaki Sekine, Rie Matsumoto, Makoto Konoto, Hitoshi Kubota, Akio Fukushima, and Shinji Yuasa, Applied Physics Express **6** (7), 073005 (2013).

[56] T. Maruyama, Y. Shiota, T. Nozaki, K. Ohta, N. Toda, M. Mizuguchi, A. A. Tulapurkar, T. Shinjo, M. Shiraishi, S. Mizukami, Y. Ando, and Y. Suzuki, Nat Nanotechnol **4** (3), 158 (2009).

[57] F. Bonell, S. Murakami, Y. Shiota, T. Nozaki, T. Shinjo, and Y. Suzuki, Applied Physics Letters **98** (23), 232510 (2011).

[58] U. Bauer, M. Przybylski, J. Kirschner, and G. S. Beach, Nano Lett **12** (3), 1437 (2012).

[59] Kim Woojin, J. H. Jeong, Y. Kim, W. C. Lim, J. H. Kim, J. H. Park, H. J. Shin, Y. S. Park, K. S. Kim, S. H. Park, Y. J. Lee, K. W. Kim, H. J. Kwon, H. L. Park, H. S. Ahn, S. C. Oh, J. E. Lee, S. O. Park, S. Choi, H. K. Kang, and C. Chung, Electron Devices Meeting (IEDM), 2011 IEEE International, 24.1.1 (2011).

[60] H. Sato, M. Yamanouchi, K. Miura, S. Ikeda, R. Koizumi, F. Matsukura, and H. Ohno, Magnetics Letters, IEEE **3**, 3000204 (2012).

[61] Hao Meng, Vinayak Bharat Naik, Ruisheng Liu, and Guchang Han, Applied Physics Letters **105** (4), 042410 (2014).

[62] Yoichi Shiota, Shinichi Murakami, Frédéric Bonell, Takayuki Nozaki, Teruya Shinjo, and Yoshishige Suzuki, Applied Physics Express **4** (4), 043005 (2011).

[63] L. Liu, C. F. Pai, D. C. Ralph, and R. A. Buhrman, Phys Rev Lett **109** (18), 186602 (2012).